A Portable Non-Invasive Electromagnetic Lesion-Optimized Sensing Device for the Diagnosis of Skin Cancer (SkanMD)

Nader Shafi, Joseph Costantine , *Senior Member, IEEE*, Rouwaida Kanj , *Senior Member, IEEE*,
Youssef Tawk , *Senior Member, IEEE*, Ali H. Ramadan , *Member, IEEE*, Mazen Kurban, Jihane Abou Rahal,
and Assaad A. Eid

Abstract—The article presented herein proposes an alternative skin cancer screening method that delivers non-invasive diagnosis and monitoring of skin lesions by leveraging electromagnetic waves with radio frequency technology and circuits. The proposed hand-held device, named SkanMD, comprises a sensitive electromagnetic sensor, customized radio frequency wave analyzer circuits, and machine learning algorithms. The device is used in clinical studies that are performed on a total of 46 individuals that are composed of 18 patients with pre-diagnosed skin cancer, 10 individuals with benign nevi, 7 patients with arbitrary diseases, and 11 healthy individuals. These studies included the measurement of the reflection coefficient, S11, on multiple skin regions and recording the obtained complex values to build a Support Vector Machine (SVM)-based classification model. Due to the lesion-optimized sensor and the unified cross-patient classifier, our results differentiate between cancerous and non-cancerous skin lesions with a sensitivity that exceeds 92% and a specificity that exceeds 81.4%. These reported results are based on a limited population size study. They also demonstrate that SkanMD is a promising solution that could augment conventional diagnosis methods to greatly improve patient comfort and enable instantaneous and accurate diagnosis.

Index Terms—Electromagnetic sensor, machine learning, non-invasive, skin cancer, wave analyzer.

I. INTRODUCTION

SKIN cancers are among the most prevalent types of cancer, while also counting as some of the most dangerous forms of skin anomalies [1]. Skin cancer can be divided into two categories, non-melanoma and melanoma. Non-melanoma skin cancers (NMSCs) are mainly Basal Cell Carcinoma (BCC) and Squamous Cell Carcinoma (SCC) which are often non-lethal and comprise the largest portion of skin cancers [2]. Screening for skin cancer often includes surgical intervention to confirm the diagnosis, which can be uncomfortable and potentially disfiguring [3]. Notably, the world health organization estimates that 2 to 3 million non-melanoma and more than 130,000 melanoma cancers occur globally each year [4]. It is needless to emphasize that early diagnosis of skin cancer and timely intervention increase the chances of successful treatment and enhance the rate of survival [5].

Currently, skin cancer is primarily diagnosed using subjective approaches such as visual inspection, which highly depends on the experience of dermatologists and practitioners. Fig. 1 presents some of the common anomalies that require further examination to deduce malignancy. In addition, dermatologists often rely on invasive procedures such as the biopsy, which is considered the gold standard in determining the malignancy of a tumor. Notably, the biopsy procedure remains discomforting, scarring, and may result in complications for the patient [6], [7], [8], [9], [10], [11], [12]. Due to the inconvenient, subjective, invasive, and time-consuming nature of skin cancer diagnosis, many researchers have explored the potential of relying on non-invasive means for the characterization of healthy and anomalous skin, such as bio-electrical impedance, machine learning-based image classification, and electromagnetism-based (EM-based) techniques to diagnose a variety of skin anomalies [13], [14], [15], [16], [17], [18], [19], [20], [21], [22], [23]. EM and bio-impedance techniques exploit the differences between the electrical properties of healthy and suspicious lesions (dielectric permittivity) which cause a notable difference in the magnitude and phase of the transmitted and reflected electrical signals. EM-based techniques often employ structures such as waveguides, coaxial probes, radars, and multi-antenna systems operating within the microwave or millimeter wave (mm-wave) portion of the frequency spectrum. These techniques characterize human
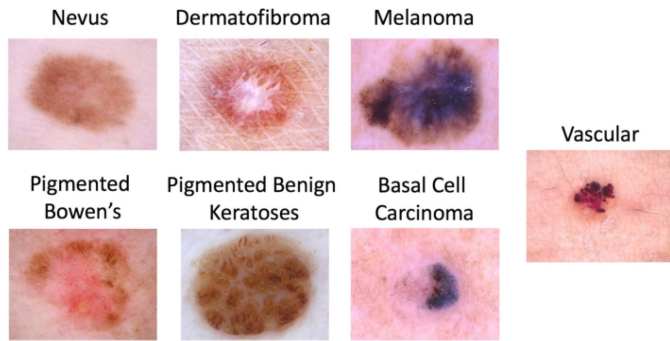
Fig. 1. A variety of skin anomalies [28].

Fig. 2. An illustration of examining a cancerous skin lesion with the proposed EM sensor.

skin permittivity at different frequency spans and leverage EM principles to differentiate between healthy and anomalous skin lesions, which have been proven to possess different dielectric properties as detailed in [17], [20], [21], [24]. These studies, which concluded with statistically significant differences between the devices' physical responses to healthy and anomalous skin, highlight the ability of EM-based techniques to sense skin abnormalities safely and non-invasively.

On the other hand, machine learning and artificial intelligence techniques, which have gained significant interest in the recent years, are dedicated to classifying and diagnosing skin anomalies based on images of the suspected lesions [14], [15], [16], [25], [26]. Accuracies comparable to the visual inspection of dermatologists and general practitioners have been reported. Such techniques typically rely on Convolutional Neural Networks (CNNs), a well-known deep learning algorithm used to identify skin cancer patterns through images, and provide a diagnosis accordingly [14]. However, the authors in [27] revealed that alterations in color balance due to non-standardized lighting conditions as well as the orientation of the photos can lead CNNs to produce false results, therefore resulting in significant misclassification. This drawback further emphasizes the need for a completely objective method of sensing that is immune to all non-intrinsic variables of skin cancer.

In this work we propose a novel, portable, real-time, and low-cost sensing system tailored for the accurate detection of skin cancer by relying on a highly sensitive electromagnetic sensor, a custom wave analyzer circuit, and machine learning algorithms that rely on the EM sensor's physical responses to assess the risk of the skin anomaly. Fig. 2 illustrates the application of our non-invasive EM sensor on top of a cancerous skin lesion. The proposed system relies on detecting the variations between the dielectric properties of healthy and diseased skin using electromagnetic waves. Subjective features, such as color, size, orientation, and lighting conditions are effectively invisible to electromagnetic waves, therefore we enforce and guarantee the sensing of the intrinsic skin properties without interference. The proposed system overcomes multiple challenges faced by traditional counterparts and puts forth several advantages, such as lesion-optimization via a narrow and focused beam strictly confined to the lesion being studied, external Radio-frequency (RF)/EM interference mitigation, immunity to pigmentation and lighting conditions, as well as unprecedented compactness and
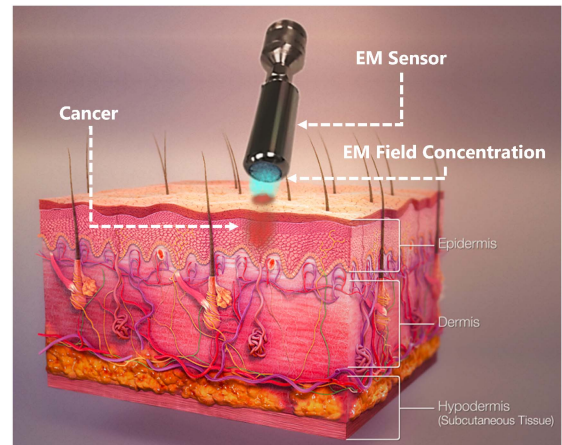
low-cost, as elaborated throughout this manuscript. The system has been clinically studied on skin cancer patients among others, and the results have successfully shown a significant ability to detect skin cancer non-invasively. The novelty of the proposed system is divided into multiple aspects. The first aspect of novelty resides in presenting a complete and stand-alone system that is clinically validated for skin cancer detection. The second aspect relates to the specific design of the sensor, which is characterized by a lesion-shape optimized topology that enables a better resolution in sensing very small skin lesions. The third aspect of novelty relates to the frequency operation of the system which can span from 2.3 GHz to 6 GHz controlled and driven by one back-end circuitry. Such wide frequency potential unlocks the possibility of expanding the future capability of this device to offer more flexibility in the penetration depth to track the skin lesions in depth and width in addition to the ability to switch between various frequencies to identify different dielectric signatures of other diseases. The last novelty aspect relates to the miniaturization of the entire system, which enables the swift and easy implementation of such skin cancer detection system.

Section II of this paper provides the theoretical background behind the interaction of EM waves with different materials, and specifically skin. Section III details the concept and design of the proposed system, including the EM sensor, the wave analyzer, and the corresponding algorithms. Section IV presents the system's measurements and results. Section V concludes the work presented and discusses clinical significance.

II. THEORETICAL BACKGROUND

The complex relative permittivity of biological materials such as skin, blood, among other tissues dictates the behavior of the biological material under exposure to an electric field [29]. The permittivity is typically given by (1) [30], where the real part is defined as the dielectric constant, and the complex part is defined as the dielectric loss factor.

$$\epsilon_r = \epsilon'_r - j\epsilon''_r \tag{1}$$

ϵ_r is the complex permittivity, ϵ_r' is known as the dielectric constant and ϵ_r'' is the complex part.

The sensing indicators can be a shift in the resonant frequency or a change in the magnitude or phase of scattering parameters [30]. One of the unique features proposed in this work herein is its single-port operation. In our one-port approach, we rely on the reflection coefficient, or S_{11}. Within this context, the S_{11} is a measure of the power reflected from a sensor operating at radio-frequency (RF) after being excited with a source RF signal. Upon the introduction of a specimen with dielectric properties to the sensing device, the emanating electric and magnetic fields are perturbed by the specimen's properties. This is known as the "Perturbation Method" which is typically used in material characterization and thoroughly discussed in [31].

The above abstraction is utilized as the underlying foundation of our study and technique, which can be summarized as: the electrical properties of skin tissues can alter the behavior of electromagnetic structures, such as sensors. Such sensors generate electromagnetic fields that are perturbed by the presence of a specimen under test (SUT) of a characteristic permittivity, such as skin, which is represented by a change in the sensor's S_{11}. Such characteristics of biological materials and their interaction with EM waves are thoroughly studied and described in [20], [32], [33], [34]. Specifically, variations in the permittivity of skin due to several factors, such as disease, humidity, and dryness cause the response of the sensor to shift from a baseline corresponding to healthy skin. Throughout the literature, it has been proven that diseases such as cancer change the dielectric properties of skin, and hence, cause the behavior of a sensing structure to shift accordingly [17], [18], [24], [35]. By studying such shifts and the associated trends, one can ultimately conclude characteristics that are representative of the disease. A plethora of work in the literature has verified that, indeed, statistically significant dielectric differences are present between healthy, benign, and cancerous skin, allowing for the conception of methods that aim to diagnose skin cancer by means of electromagnetic technology. For example, the work presented in [24] executes an ultra-wide-bandwidth study of the dielectric properties of freshly excised healthy skin and malignant tissues such as BCC and SCC cancers. The experiment is carried out by means of a typical open-ended coaxial probe as the electromagnetic structure performing the measurement. After analyzing the dielectric properties of these excisions, the study concludes with the existence of statistically significant differences in the dielectric properties of malignant and healthy tissues. It is also concluded that the varying water and protein content within BCC and SCC was the cause of variation in the dielectric properties. Furthermore, the work presented in [35], [36] also illustrates the ability of EM waves to differentiate between healthy and malignant tissues by relying on an ultra-wideband synthetic imaging system. This system is tested on a variety of skin lesions, and was successful at differentiating between malignant and benign lesions based on their electromagnetic reflectivity.

The proposed work exploits these fundamentals to produce a unique response from the proposed system which highlights the distinct properties of the SUT (whether a cancerous or a healthy one) non-invasively.

III. THE PROPOSED SYSTEM

A. The Lesion-Optimized EM Sensor

The design of a specialized microwave sensor for skin cancer detection must possess multiple features that are pivotal to its ability to differentiate between healthy and cancerous skin with heightened resolution at a practical stand-off distance. These features include enhanced sensitivity to skin lesions, immunity to environmental factors, optimal design for lesion geometry, and minimal signal distortion. The proposed sensor is a planar microstrip resonator with a length equivalent to a half wavelength ($\lambda/2$) at a frequency of 4.75 GHz (Fig. 3). The developed sensor utilizes the high performance RT Duroid 5880 substrate [37] having a thickness of 0.79 mm, a dielectric constant of 2.2, and a loss tangent of 0.0009. We designed, validated, and optimized the sensor using the Ansys Electronics Desktop (HFSS) electromagnetic fields solver [38]. The sensor is composed of two sections: a resonant element and an impedance matching network. The optimized sensor design resulted in an 85 ohms resonant element that corresponds to a narrow 1 mm-wide microstrip line, which increases the quality factor, and equivalently, the sensitivity. In addition, this element is 19.825 mm long, which corresponds to the optimized half wavelength at 4.75 GHz. Consequently, the matching network matches the sensor's impedance to the standard feeding impedance of 50 ohms. The matching network comprises a 4.5 mm long microstrip line with a 40 ohms characteristic impedance, along with a 1.2 mm long open shunt stub section having a characteristic impedance of 35 ohms. Furthermore, the 40 ohms microstrip line is tapered to further optimize the impedance matching. This procedure results in a well-matched sensor that is fabricated and assembled. The overall dimensions of the assembled sensor within its enclosure are 31 mm x 11.8 mm x 6 mm. In addition, the sensor's operation within the microwave region of the frequency spectrum (4.75 GHz), a form of non-ionizing radiation, ensures the safety of our technique when compared to other forms of radiation such as X-rays [39]. This frequency is chosen as a trade-off between both the sensor and circuitry's size and cost. Primarily, utilizing a lower frequency would physically increase the size beyond what is considered portable (due to the dependence on the wavelength of the frequency used) and makes the sensor design significantly more challenging when aiming to focus EM waves on very small regions (skin lesions). On the other hand, going higher in frequency would incur much more complex and costly circuitry while miniaturizing the sensor beyond practical convenience. From an electromagnetics perspective, 4.75 GHz falls within what is known as the gamma region [33], which means the biological changes detected by the sensor are due to water, and proteins, among other constituents of the specimen, which is suitable for cancer detection. Notably, the sensor adheres to the regulations adopted by the Federal Commissions Committee (FCC) to limit radiation emission levels as stated in ANSI/IEEE C95.1-1992 [40]. The proposed sensor achieves a peak SAR of 0.1 W/Kg at its operational input power of -15 dBm, which is well below the critical SAR threshold.

Traditional EM sensors typically face challenges related to: 1) Low density of EM fields interacting with the SUT due to the fact that the evanescent fields are majorly confined within the
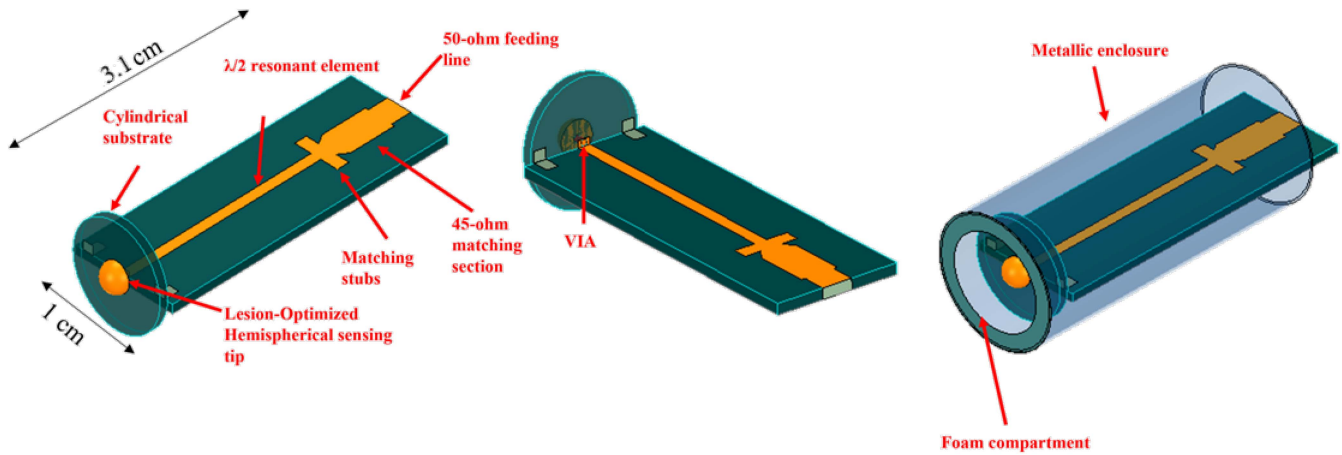
Fig. 3. The lesion-optimized topology, and the dimensions of the proposed EM sensor along with the designed metallic enclosure.
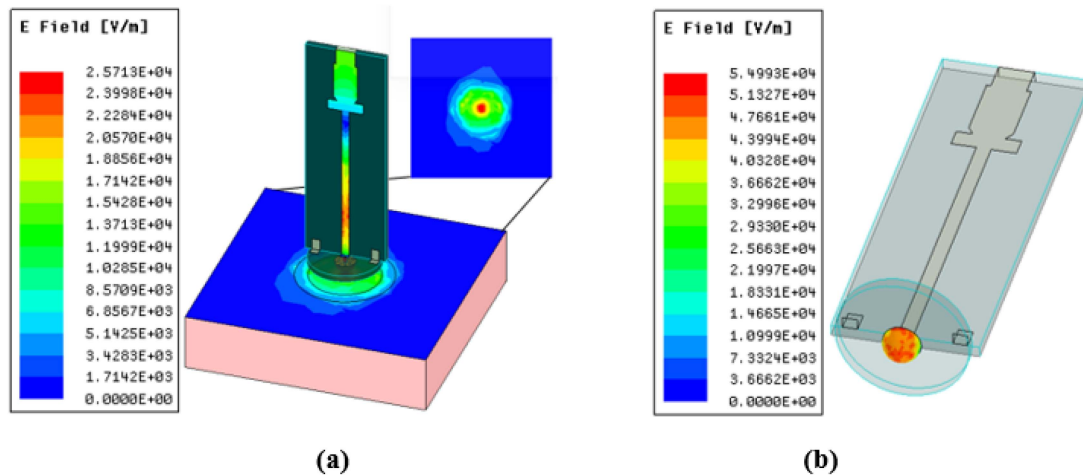

Fig. 4. (a) The E-Field distribution along the length of the sensor's resonant element. (b) The high E-Field concentration at the hemispherical sensing tip highlights its sensitivity at this region.

substrate material of the sensor instead of being concentrated near the SUT [23], [41]; 2) Significant dependence on the stand-off distance (the distance between the sensor's active region and the SUT) which means that slight variations in this distance are capable of noticeably changing the sensor's response; 3) Large sensors or impractical circuitry due to extremely high cost and difficult mobility. The proposed sensor addresses these challenges simultaneously.

First, we achieve a significant sensitivity by: 1) Implementing a narrow line topology to achieve a higher quality factor. The higher quality factor, and equivalently the exhibited narrow bandwidth of operation allows for the detection of finer dielectric changes within the SUT that otherwise would have been shadowed by the bandwidth of a wide-band sensor [42]; 2) Actively integrating part of the resonant element and its emanating fields into the sensing procedure, which results in stronger and denser electromagnetic fields at the sensing tip when compared to other techniques involving evanescent-field fringing. This is achieved by extending the length of the planar resonant element into a hemispherical tip of 1 mm diameter, which is incorporated into

a cylindrical substrate of 5 mm radius and 0.79 mm thickness, as shown in Fig. 3.

In Fig. 4(a) we present the electromagnetic simulation of the electric field (near E-field) intensity distribution along the sensor, and in Fig. 4(b) we present the concentration of the E-field at the hemispherical sensing tip. The peak magnitude of the E-field at the surface of the hemispherical tip is $5.5 * 10^4$ V/M, more than twice the peak magnitude along the resonant element ($2.571 * 10^4$ V/M). These simulations attest to the success of our approach in focusing the EM waves at the hemispherical tip where the skin of the patient will be positioned. Additionally, Fig. 4(a) highlights the confinement of the sensing area at a stand-off of 0.6 mm, where the maximum illumination region, and therefore sensitivity (highlighted in red), is directly beneath the hemispherical tip in a circle of radius r = 1 mm (an area of $\pi \ mm^2$), and the full-width at half-maximum (FWHM) is approximately 3 mm (an area of 28.3 mm^2). Furthermore, the sensing depth is analyzed by evaluating the normalized near E-field at several distances from the sensor's tip, as shown in Fig. 5(a). Notably, the normalized E-field is significantly reduced
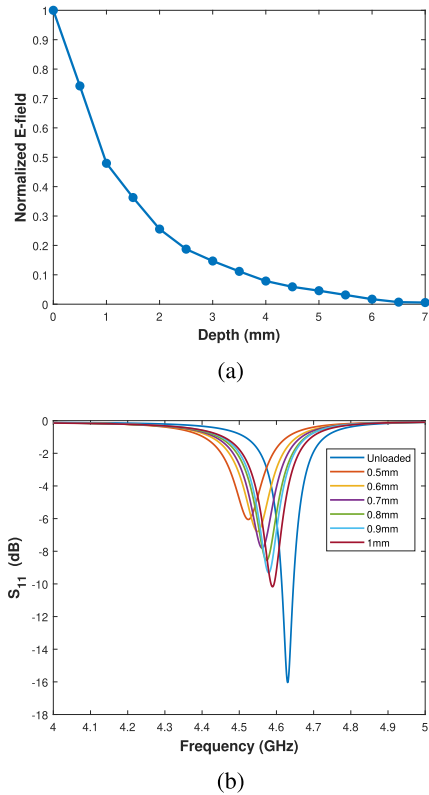
(a)

(b)

Fig. 5. (a) presents the normalized magnitude of the E-field and its decreasing intensity within a SUT to highlight its sensing depth. (b) presents the effect of the stand-off distance on the response of the sensor (sensitivity) in terms of the S_{11} and the frequency shift.

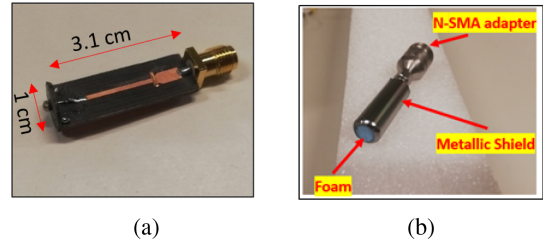
(a)   (b)

Fig. 6. (a) The fabricated EM sensor. (b) The fabricated EM sensor is assembled within its metallic enclosure.

Fig. 7. The EM sensor's measured and simulated S_{11}.

at 3.5 mm and vanishes completely beyond 6 mm. Additionally, the sensitivity degradation incurred by the stand-off distance is also studied. In Fig. 5(b), we simulate the sensor's S_{11} initially at an unloaded state (without adding a skin-mimicking layer) and at a skin-loaded state with increasing stand-off distances in steps of 0.1 mm. At a stand-off distance of 0.5 mm, we can observe an 85 MHz frequency shift and a 6.7 dB decrease in the S_{11} from the initial unloaded state (4.631 GHz and -16 dB). As the stand-off increases, the frequency shifts, and the change in S_{11} decreases. At 1 mm stand-off, the frequency shift decreases to 9 MHz, and the S_{11} changes by 0.8 dB. Furthermore, the geometry of the sensing tip is chosen to conform to the lesion's topology, suiting the natural geometry of the anomaly by adopting the hemispherical shape that enables a high sensing resolution for small cancerous lesions, which are typically larger than 1.5 mm. When this sensor is positioned directly above a SUT, the interaction of the E-field emanating from the hemispherical tip with the SUT is maximized. This interaction between the E-field and the SUT manifests itself as a unique response from the sensor upon the perturbation of its concentrated fields by the nature and composition of the SUT.

Second, this sensor's miniature microstrip-based topology with lesion-optimization guarantees an accurate measurement of the suspected region without being influenced by the adjacent healthy skin. The latter can happen consequently to using relatively large sensing apertures in other electromagnetic

technologies, such as coaxial probes, waveguides, and radars which are physically and electrically larger. Third, a metallic shield is designed and fabricated to the dimensions of the sensor, which immunizes it to environmental radio frequency (RF) noise such as WiFi signals among others. Furthermore, such a shield provides a stable fixture that maintains the desired separation distance. The metallic shield is a conductive enclosure which prevents interaction with the ambient electromagnetic waves while simultaneously thwarting sensing from undesired skin regions. This enclosure includes a cutout at the sensing tip's location, where the desired sensing will be performed. Furthermore, the shield incorporates a compartment that fits a hard-foam spacer between the sensing tip and the SUT. Hence, a fixed separation distance is ensured, and the flatness of the underlying skin is preserved. The fabricated sensor prototype is shown in Fig. 6(a), it is fitted inside its shielding enclosure in Fig. 6(b). After fabrication, the sensor's operation is validated by measuring its S_{11} using a Vector Network Analyzer (VNA) [43]. It is shown in Fig. 7 that the measured and simulated S_{11} are in great agreement. Additionally, the observed narrow bandwidth of operation also verifies the high quality factor required for sensing small dielectric differences.

B. The WaveWhisperer

The second major component of the proposed sensing system is the backend wave analyzer that we name "WaveWhisperer". This component is the "brain" of our proposed system that interrogates the sensor, which in turn examines the skin. Technically,
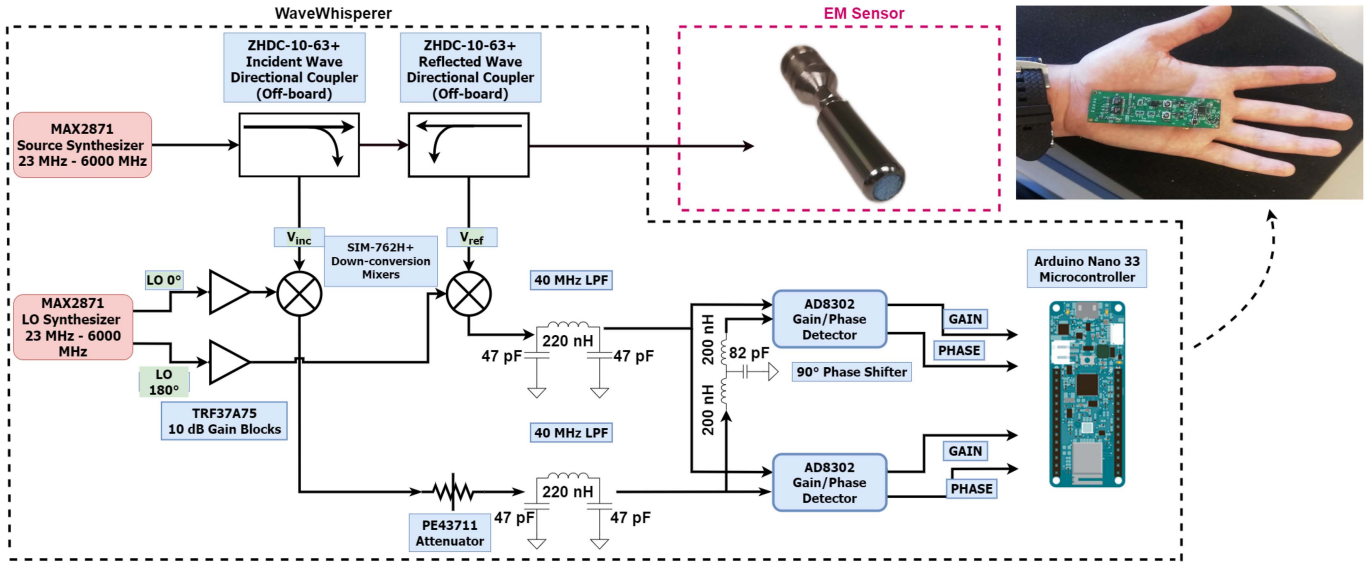
Fig. 8. The block diagram of the WaveWhisperer's architecture, in addition to showing a fabricated receiver module within the palm of the hand.

this wave analyzer generates the stimulus signals transmitted to the sensor, analyzes the reflected signals in the measurement procedure, extracts the S_{11} magnitude and phase, and executes tailored learning algorithms on the obtained on-skin measurements for the detection of malignancy. This device is a new, customizable, portable, compact, and cost-efficient analyzer that operates from 2.3 GHz to 6 GHz and it is also WiFi connected for practicality. A VNA is typically used for generating and analyzing transmitted and reflected signals from a variety of high frequency devices and structures such as antennas and sensors. Although a traditional VNA serves multiple and more comprehensive functions other than measuring the S_{11}, the proposed wave analyzer is custom-made, and it overcomes the size, power, and cost constraints of a traditional VNA for this specific task of measuring the complex S_{11} of a sensor within the specified frequency range without the extra functions and the standard metrology-level measurement accuracy. Hence, in addition to providing a highly sensitive EM sensor, we also present an alternative wave analyzer that achieves suitable performance characteristics for integration within portable and compact medical devices. Essentially, the design decisions should achieve a device capable of measuring the lowest magnitude of S_{11} of our sensor in free-space, which is between -20 dB to -25 dB. Fig. 8 presents the complete block diagram of the WaveWhisperer. The fabricated prototype of the receiver module is shown in Fig. 9(a) where the different stages are labeled, and Fig. 9(b) presents the backside of the receiver module where the microcontroller resides. Also, Fig. 9(c) presents the front side of the transmitter module, which is only populated with the synthesizer IC. The bottom side of the transmitter module can have an optional microcontroller attached or left unpopulated.

We designed the printed circuit board (PCB) of the analyzer circuit based on a 4-layer stack-up using KiCad [44]. This is the typical standard for high-performance RF and mixed signal circuitry. Such a stack-up allows for better isolation between high-frequency signals, power planes, and external interference.

(a)

(b)

(c)
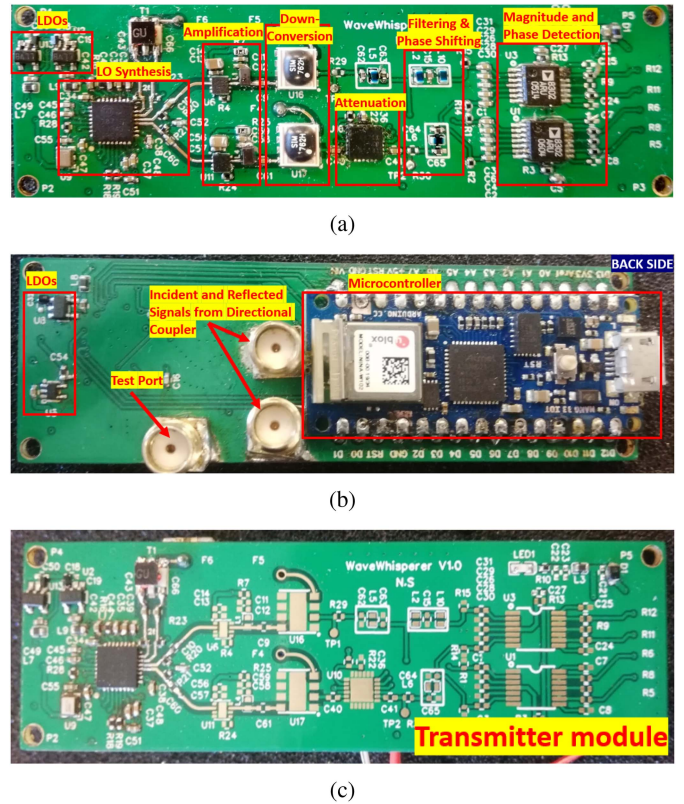
Fig. 9. (a) and (b) present the front and back sides of the fabricated and assembled receiver module of the WaveWhisperer; (c) presents the populated side of the transmitter module.

This PCB connects the signal and power traces in-between and to the various components forming the network analyzer circuitry. The 4-layer PCB was fabricated at JLCPCB according to the technology offered in [45]. The signal in the WaveWhisperer is initiated by a source, known as the frequency synthesizer,

MAX2871 from MaximIntegrated. This source is capable of synthesizing frequencies from 23.5 MHz to 6 GHz, and in our device we utilize frequencies from 2.3 GHz to 6 GHz. The source is fabricated onto a separate WaveWhisperer PCB (a transmitter module that only includes the soldered synthesizer IC). Additionally, this source is programmed via SPI through the on-board microcontroller to mimic a VNA sweep. Since we utilized the VNA to sweep a 1 GHz bandwidth from 4 GHz to 5 GHz (encompassing the used sensor's frequency of operation) at 1001 points, we also program the synthesizer to sweep this 1 GHz bandwidth in steps of 1 MHz (1001 points). This frequency step is made possible by using a high frequency temperature-compensated crystal oscillator (TCXO) operating at 40 MHz from Kyocera (KT2520 K). This oscillator is chosen to reduce the effects of temperature changes on the stability of the frequency feeding the synthesizer. The output of the source is connected to two high directivity (>30 dB) directional couplers from MiniCircuits (ZHDC$-10-63+$) connected in series, whose purpose is to couple portions of the incident and reflected signals propagating towards and from the sensor, respectively. These two coupled signals are of high-frequency content and must be down-converted to enable more convenient processing. Consequently, we utilize two double-balanced mixers from MiniCircuits (SIM-762H+) to down-convert the reflected and incident waves simultaneously to a lower intermediate frequency (IF). These mixers operate from 2.3 GHz to 6 GHz and are capable of down-converting a signal to a frequency ranging from DC to 3 GHz at a typical conversion loss of 6 dB. For these mixers to operate, another source labeled as the Local Oscillator (LO) (another MAX2871) must be used to drive them. Similar to the first source, we program the LO to always operate at 40 MHz lower than the source frequency in order to arrive at a 40 MHz down-converted signal ($f_{IF} = f_{Source} - f_{LO}$). Additionally, the LO signals that are typically 3 dBm in power are fed to two gain blocks to increase their power before entering the mixers. The used gain blocks are from Texas Instruments (TRF37A75) that provide a 12 dB gain over a wide frequency range from 40 MHz to 6 GHz. After down-conversion, the signal in the reflected path passes through a custom-made Pi-type low-pass filter to block undesired harmonics and intermodulation products from propagating into the detector. This filter is achieved by connecting two 47 pF capacitors and a 220 nH inductor in a Pi configuration. The filter is designed and simulated in ADS [46]. On the other hand, the signal in the incident path passes through an attenuation stage by means of a programmable attenuator from pSemi that enables attenuation from 0.25 dB to 31.75 dB (PE43711). This attenuation stage allows us to perform signal-balancing to avoid a large difference in the power of the reflected and incident signals once fed to the detectors that specify a maximum difference of 30 dB. Similarly, this signal also passes through an identical LPF as in the reflected path. Both the reflected and incident signals enter two magnitude and phase detectors from Analog Devices (AD8302) which output the difference between two signals in terms of magnitude and phase. The detectors can measure a signal as low as -60 dBm. It must be noted that the detectors can output a phase difference ranging from 0 to 180 degrees and

cannot output the full 0–360 degrees range on their own. For this reason, the signal in the reflected path is split into two, where one of the paths undergoes a 90 degrees phase shift by means of a custom T-type LPF and enters one detector along with half the signal from the incident path, while the other unshifted half enters the second detector along with the second half of the incident signal. This phase shifter is designed using two 200nH inductors and one 82 pF capacitor. Additionally, this approach is known in the user community of this detector and allows us to obtain the full phase range. Finally, the microcontroller reads the analog voltages from the two detectors and maps them to their magnitude (dB) and phase (degree) counter-parts. These voltage differences correspond to the voltage ratios between the reflected and incident signal, which represent the reflection coefficient or S_{11} that we are seeking. These calculations are performed within the microcontroller. To energize the entire system, we utilize four low-dropout regulators (LDO regulators) that take the 5 V Arduino (Nano 33) input (USB voltage) and output steady voltages required by the frequency synthesizers and the crystal oscillator. Three of these regulators are from Texas Instruments (LP5907), which transform the 5 V input into three 3.3 V outputs to supply the synthesizers, which is the recommended best practice approach suggested by the manufacturer. These regulators are specifically chosen due to their low-noise specification which is essential when supplying phase-locked loops in frequency synthesizers. On the other hand, another regulator from Microchip Technologies (MIC5366) is chosen to supply the crystal oscillator by transforming the 5 V input to a 1.8 V output. The 4-layer design significantly contributes in reducing the size of the whole system due to the additional routing and assembly space. Each of the 4 layers in the WaveWhisperer serves a designated role, as follows: Layer 1 - contains RF transmission lines and high-speed signals. Layer 2 - a continuous ground plane. Layer 3 - a power plane containing the 3.3 V and 1.8 V supply lines. Layer 4 – an additional signal and ground layer.

The entire system is powered by a 5 V output from the Arduino module which can either be powered by means of a USB cable connected to a personal computer or a battery. The maximum power consumption of the WaveWhisperer is 2.5 W during measurement collection where the output powers of all synthesizers is chosen as the highest option (5 dBm). It is essential to note that measurement collection is momentary, typically lasting about 1 minute, after which the synthesizers are put into sleep-mode while the gain blocks and attenuator are turned off, thereby reducing the power consumption to a maximum of 0.61 W. The prototype is capable of being fully wireless by attaching a battery instead of the USB for power and using the microcontroller's on-board WiFi and Bluetooth support for transmitting the data and receiving commands. We validate the performance of the WaveWhisperer by connecting it to a personal computer via USB. The entire system is shown in Fig. 10 and a close-up of the WaveWhisperer is shown in Fig. 11. The design decisions of the WaveWhisperer resulted in a scan time of approximately 8 seconds, and a noise figure of approximately 14 dB. These results satisfy our design requirements comprising a short scan time (less than 2 minutes), a sufficient noise figure that does not
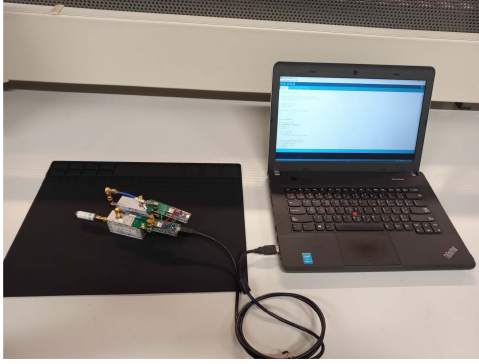
Fig. 10. The full measurement setup including the WaveWhisperer connected to the proposed EM sensor and controlled via laptop.
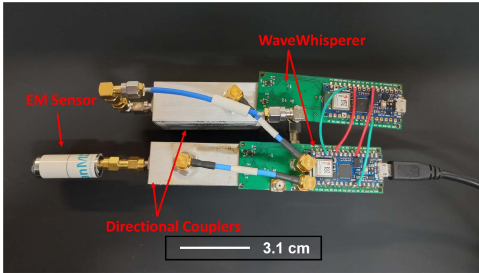

Fig. 11. A close-up of the connected system showing the transmitter and receiver modules of the WaveWhisperer, the directional couplers, and the EM sensor.
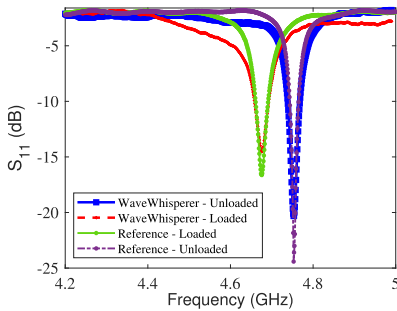

Fig. 12. The WaveWhisperer's measured S_{11} for a skin loaded/unloaded measurement with an overlay from a reference VNA from Keysight [43].

degrade the incident and reflected signals (which are larger than -50 dBm), and the ability to measure the lowest magnitude of S_{11} in the range of -20 dB to -25 dB. Additionally, the frequency stability of the device is primarily governed by the TCXO's 2.5 ppm stability which results in around $\pm (5\text{–}15)$ KHz at the boundary frequencies of 2.3 GHz and 6 GHz, respectively. Such variations have insignificant effects on our sensing and frequency resolution since the bandwidth and sensitivity of the sensor in addition to the intermediate frequency (IF) chosen (1 MHz) are orders of magnitude larger. Then, the EM sensor is connected to the WaveWhisperer through a coaxial connector, and S_{11} measurements are executed.

First, we measure the S_{11} of the sensor in an unloaded free-space state (not on skin). Then, the sensor is loaded with the skin and the S_{11} is measured. Fig. 12 shows the success of the
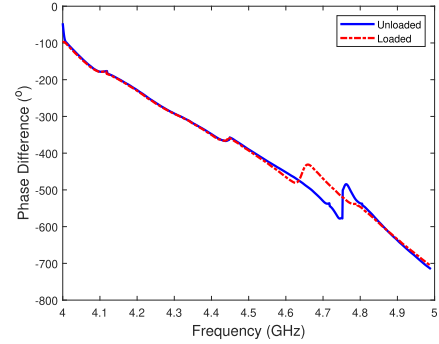

Fig. 13. The full unwrapped phase range between a loaded and unloaded measurement on skin.

WaveWhisperer in producing the sensor's S_{11}, both in the loaded and unloaded states, where the observed shift in frequency and magnitude confirm the expected response, as verified by the VNA reference overlays. Additionally, we implemented a digital LPF FIR filter to eliminate the high-frequency noise from the signal, and therefore produce the aforementioned S_{11} plot. The FIR filter samples the signal at 9 KHz and is composed of 33 taps. The filter produces optimal results at a cut-off frequency of 1 KHz. Similarly, we produce the S_{11}'s unwrapped phase angle in both skin loaded/unloaded states in Fig. 13. The obtained results clearly validate the performance of the WaveWhisperer and its ability to produce the complex S_{11}, satifying the requirements of our application.

C. Study Design and Statistical Analysis

1) Data Collection: We use the proposed EM sensor to perform measurements on the skin of patients and healthy volunteers, totaling 46 individuals. The sample size was chosen based on the availability of patients, their willingness to participate, and the COVID restrictions. Then, we record the observed complex S_{11} (magnitude and phase). We perform these measurements by placing the sensor on the skin and ensuring light contact between the foam spacer and the lesion. The recorded S_{11} is key to understanding the nature of the SUT, especially since the unique composition of a specimen dictates its complex permittivity, which in turn governs the unique variation in the sensor's S_{11}. For each specimen, whether healthy, benign, or diseased, 1001 complex S_{11} points – each corresponding to the frequencies from 4 GHz to 5 GHz in steps of 1 MHz – are captured and replicated 10 times while maintaining continuous contact. This frequency range encompasses the sensor's frequency of operation. Once the data from the designated locations is obtained, it is then categorized and labeled based on the skin's nature, dimensions, and locations. This results in a set of S_{11} magnitude and phase measurements for each measurement class (healthy, benign, arbitrary, cancerous) on the two examined locations per everyone, which forms the differential pair.

After observing the measured S_{11} over the entire frequency range (4 GHz – 5 GHz), we notice that a specific range within the entire bandwidth is significant for analysis. Particularly, the S_{11} data of the skin-loaded sensor within a bandwidth of

141 MHz, centered at the resonance frequency of the sensor, experienced significant changes in the S_{11} magnitude and phase. Therefore, we extract 141 points, corresponding to the desired bandwidth from the original spectrum. The resultant is a bandwidth containing valuable measurements that will be further analyzed and used for building our classification model. This procedure is then repeated for the healthy volunteers on pairs of data corresponding to adjacent healthy locations (e.g.: Temple1, Temple2, Forehead1, Forehead2). It is important to note that data for training and testing are shuffled at each iteration to ensure randomization. Additionally, the study was conducted with the operators and examiners being aware of everyone's case. However, the built model, as discussed in the next section, is blind to the samples passed for testing and validation, i.e., we evaluate the trained model with the testing data without passing their labels and then examine the diagnostic output of the model.

2) Wrapper-Based Multi-Feature Analysis of the Frequency, Magnitude, and Phase of the S_{11}: In building our model, we rely on dual measurements, which are obtained for the samples of cancer patients, healthy individuals, benign nevi, and arbitrary diseases to extract a feature set (S_{11} magnitude and phase values at specific frequencies) that will be used to develop a corresponding classification model. Common to all test scenarios, we adopt a two-class classification model. Our learning model expects two classes, cancerous and non-cancerous, and we herein, refer to class 1 as the skin cancer class, and class 2 changes depending on the specific scenario. The statistical significance of our technique is studied by developing and evaluating three case study scenarios. These scenarios comprise evaluating three data groups that combine different measured samples from the general population to investigate our technique's ability to distinguish between the cancer group and non-cancer groups. The scenarios are as follows: Scenario 1 – 'skin cancer' measurements vs. 'healthy skin + benign nevi' measurements (abbrev. 'SC' vs. 'H + BN'); Scenario 2 – 'skin cancer' measurements vs. 'benign nevi + arbitrary diseases' measurements (abbrev. 'SC' vs. 'BN + AD'); Scenario 3 – 'skin cancer' measurements vs. 'healthy skin + benign nevi + arbitrary diseases' measurements (abbrev. 'SC' vs. 'H + BN + AD'). Each scenario utilizes a two-class support vector machine (SVM) classifier that is trained on all patients and healthy volunteers (not individual-based SVM). Notably, SVMs are known for their robustness and use within binary medical classification [47], [48], [49], [50]. Hence, for scenarios 1, 2, and 3, class 2 corresponds to the previously defined 'H + BN', 'BN + AD', and 'H + BN + AD', respectively. For purposes of our model, we then compute the difference between the dual measurements for each individual and use this difference, Δ, obtained at different frequencies as the input feature set to the model. Hereon, we refer to the difference obtained for class 1 individual patients as Δ_{HC}, and the data based on the difference of the dual measurements that comprise the non-cancer population as Δ_{HH}. The said differential data represent the difference in the S_{11} magnitude (ΔMAG) and phase (ΔP) for the different classes, e.g.: (ΔMAG $_{HC}$), (ΔP$_{HC}$), (ΔMAG $_{HH}$), and (Δ P$_{HH}$), as obtained from the dual measurements at multiple frequencies. This data is then passed
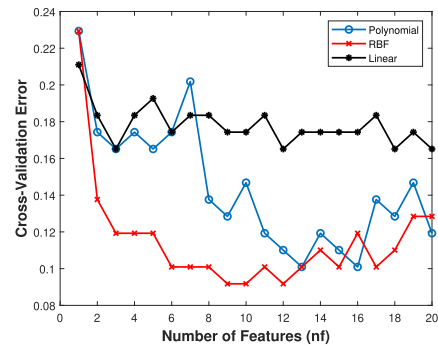

Fig. 14. The variation of the cross-validation error as a function of the number of features for each used kernel function for a specific training dataset. For this example, the best kernel function is the RBF, achieving a CV error of 0.091 at 9 features.

through a pre-processing stage for filtering and normalization, then a feature selection stage which selects magnitude and phase data at specific frequencies deemed accurate by the feature selection algorithm (Sequential Feature Selection, [51]). Furthermore, these features are then used in a classification algorithm (SVM) which produces a model capable of predicting a suspected lesion's malignancy. The wrapper, a multi-iteration process of choosing the best model based on the cross-validation error values, is then executed and evaluated. Within the multiple iterations of the wrapper, the best kernel (important parameter of an SVM) and the best feature set are identified. The best feature set is a combination of S_{11} magnitudes and phases at specific frequencies which are deemed capable of accurately classifying the measured lesion based on their cross-validation score (the lowest error). Fig. 14 presents the variation of the cross-validation error versus the number of features included in building the model. For illustration purposes, we can see that the Radial Basis Function (RBF) achieved the lowest cross-validation error at 9 "best" features for one of the scenarios. The "best features" and the "best kernel type" are then used to build the SVM model, which is then evaluated using our measurement data that is split into training and testing portions (90% training, 10% testing). We also note that the training data that is labeled cancerous has been labeled as such based on the results of the clinical diagnosis (post Moh's surgery). The evaluation comprises the computation of the most common classification performance metrics, such as model sensitivity and specificity.

D. Data Pre-Processing

First, we obtain the difference values for each concerned class, where for each individual we obtain a total of 282 features (141 points for ΔMAG and 141 points for ΔP) centered around the resonant frequency due to the high-quality factor of the sensor (narrow resonance bandwidth). Then, this data passes through a normalization and filtering stage which normalizes the magnitude and phase data and selectively omits dual measurement features (frequencies) that do not meet specific thresholds. Without loss of generality and for our purposes, noting the large observed variations, we set the thresholds to be ΔMAG > 10 dB

TABLE I
SAMPLES WITH AND WITHOUT SMOTE

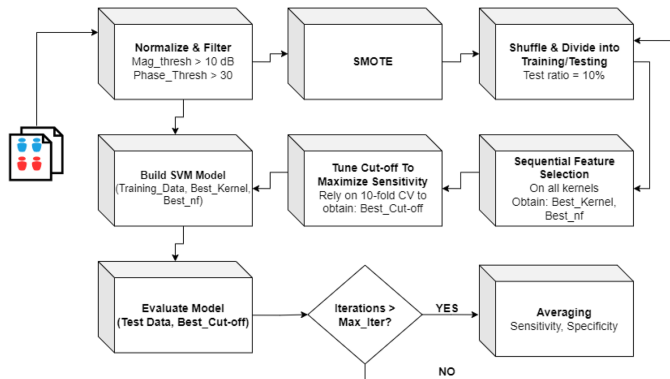| Samples	'SC' vs 'H + BN'	'SC' vs 'BN + AD'	'SC' vs 'H + BN + AD'
Without SMOTE	18 vs 54	18 vs 17	18 vs 61
With SMOTE	61 vs 61	61 vs 61	61 vs 61

Fig. 15. The block diagram of the proposed machine learning algorithm. This diagram highlights the process and data flow to reach the optimal classification model.

and $\Delta P > 30°$. To improve statistical performance, we employ the Synthetic Minority Oversampling Technique (SMOTE) [52] to synthetically increase the number of patient measurements. SMOTE is a popular algorithm for balancing different classes (minority, majority) that utilizes a distance metric to interpolate between a specified number of neighboring data points (real points), which are 4 neighbors in our case. The algorithm would therefore balance the imbalanced data, which has been shown to improve the prediction capability of a machine learning model and reduce misclassification. This algorithm is typically used in medical classification scenarios where the minority set (disease set) is lesser than the majority (control set) [48], [52], [53], [54], [55]. As an example, in [54] the authors have applied SMOTE on an imbalanced dataset of cervical cancer patients, where they have synthetically increased the patient population from 35 to 805 to balance it with the non-patient population of 823. In our application, the patient population (class 1) was synthetically increased to match the size of the largest class 2 sub-group. Since the sub-group containing the 'H + BN + AD' is the largest in size, being 61 samples, we, therefore, increase the cancer population (18) by 43 synthetic sample points to achieve balance. We also note that the 'SC' class contains the 17 BCC cases and the 1 SCC case lumped together. As for the remaining class 2 scenarios: for 'H + BN', we increase the 'BN' samples synthetically by 7 such that the size of 'H + BN' is 61, and for 'BN + AD' case (totaling 17), we increase both equally to achieve a total of 61 samples. Table I summarizes the sample populations before and after SMOTE. These balanced datasets are then randomly shuffled and divided into 90% training and 10% testing data. The procedure is repeated 10 times to obtain a good estimate of the average test error. The full statistical analysis algorithm is illustrated in Fig. 15.

IV. MEASUREMENTS AND RESULTS

A. Clinical Studies: A Differential Measurement Approach

Clinical studies are performed on a population composed of patients with pre-diagnosed skin cancer, healthy individuals, patients with benign nevi, and a selection of patients with arbitrary diseases. These studies aim to evaluate the proposed device in a clinical setting. The focus of the work is on distinguishing between cancerous and non-cancerous skin lesions, and it is imperative to reiterate that the scope of this work does not include identifying diseases other than skin cancer. Notably, the diversified population aims to introduce variability to the sensor and technique to better evaluate their performance. These studies are approved by the Institutional Review Board (IRB) committee at the American University of Beirut (Protocol DER.MK.01) [56]. Accordingly, 46 individuals participated in the measurements, including 18 patients with pre-diagnosed skin cancer, 11 healthy volunteers, 10 volunteers with benign nevi, and 7 volunteers with arbitrary diseases. In what follows, we discuss the measurement procedure for each sub-group, ultimately leading to the performance evaluation and statistical significance.

1) Measurements on Skin Cancer Patients: The patient population primarily consists of 17 BCC cases and 1 SCC case, corresponding to 50% male and 50% female participants whose ages fall between 32 and 87 years. All patients had lesions greater than 1.5 mm and smaller than 10 mm in diameter. These patients were set for Moh's surgery (defined in [57]) for the removal of their cancer and have signed the pertinent consent forms. The proposed measurement procedure consists of placing the sensor on the skin (in-vivo) and recording its resultant response afterwards in real-time. It is necessary to emphasize that during such measurements, the awareness of the effects of multiple internal and external factors on the measured properties is vital to the preservation of the quality of the measurements. These factors include body temperature, hydration, dryness, room temperature, and the introduction of any solutions to the skin. As presented within the literature, such factors are known to distort the measurements that reveal the specimen's true properties [18], [20], [32], [58], [59]. Consequently, ensuring the fidelity of our measurements has been a priority throughout our study, and thus we ensured it by introducing and adopting several protocols within the measurement process to factor in the internal and external variables. Of said protocols, dual in-vivo measurements for the differential approach are performed, since in-vivo measurements preserve the fidelity and quality of the lesion undergoing examination when compared to ex-vivo measurements. Particularly, it was revealed that the dielectric properties of ex-vivo biological specimens may differ from the specimen within its natural medium, e.g., on-body skin. These differences are especially present if the environmental and physiological conditions of the measured specimen are not properly maintained [60], [61], [62]. Furthermore, the adopted dual measurement mode comprises measurements of the cancerous lesion and its adjacent healthy tissues. Hence, for each patient, we establish a healthy baseline that the associated cancer measurement is compared to. This results in eliminating the effects of the internal and external factors common to both measured samples.
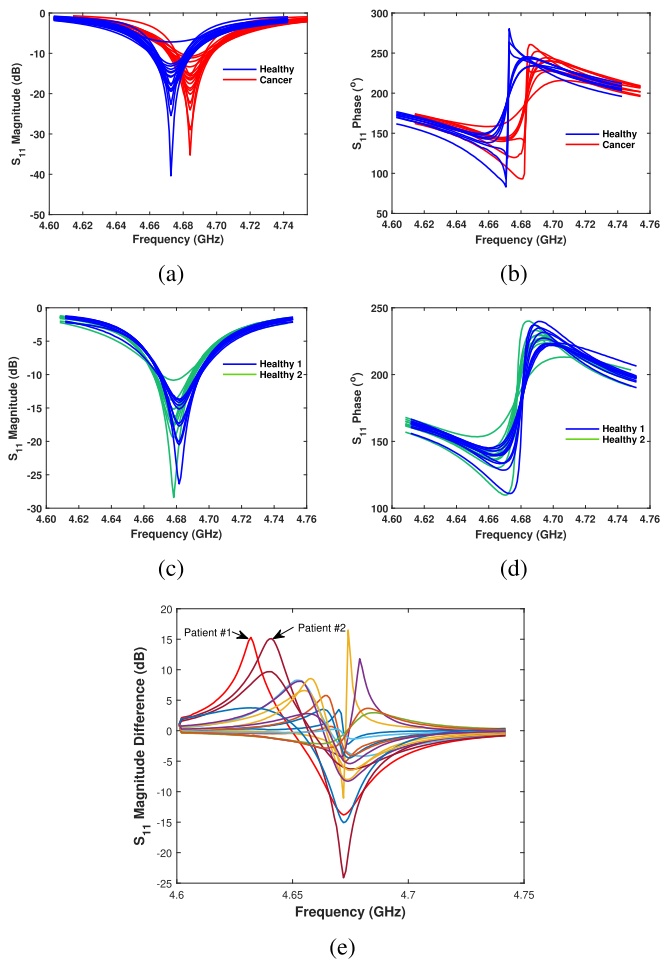
Fig. 16. (a) The measured S_{11} magnitude for all patients on their cancerous lesions and their adjacent non-cancerous skin. The cancerous and non-cancerous measurements have been centered at their average frequency shift to highlight the measured difference between both. (b) shows the measured S_{11} phase for the cancerous and non-cancerous patches for all patients, where a clear difference in the phase is observed. (c) The measured S_{11} magnitude for all healthy individuals on two adjacent patches of skin. (d) shows the S_{11} phase similarity between both healthy patches for all healthy individuals. (e) shows the difference/delta curves between the healthy and cancer S_{11} measurements of each patient to display the measurement variability across all patients without averaging.

These measurements are executed as follows: First, the sensor is positioned directly on top of the cancerous lesion, and 10 S_{11} measurements are recorded. Next, the sensor is positioned on the healthy skin adjacent to the cancerous lesions, and 10 S_{11} measurements are also recorded. These S_{11} magnitude and phase values within a specified frequency range form the "differential pair". During these measurements, a 0.6 mm-thick foam cylinder is loaded into the sensor's foam compartment to maintain a fixed stand-off distance from the SUT. Such stand-off distance and the underlying contact-less sensing are considered crucial elements in combatting the effects of different lesion topologies as well as undesired lesion fluids that may otherwise distort contact-based sensors. The tested skin cancers included in our study are located on the nose, cheeks, temples, forehead, and scalp. Fig. 16(a) presents our S_{11} measurements on the cancerous lesion and its adjacent healthy skin for all patients, where each class of measurements has been centered at the

average shifted resonance frequency of its relevant class for clearer presentation of the difference between them. Similarly, Fig. 16(b) presents the measured S_{11} phase at the cancerous lesion and its adjacent healthy skin for all patients.

2) *Measurements on Healthy Skin, Benign Nevi, and Arbitrary Diseases:* We perform the dual measurements on healthy individuals to establish a baseline reference of healthy measurements for comparison with cancer measurements. Such a reference reveals the properties of healthy skin and enables us to understand the sensor's response to healthy skin measurements. Accordingly, the executed dual measurements are performed over multiple locations of the skin for 11 healthy individuals comprising 5 males and 6 females. The measurement locations are chosen to imitate the skin cancer locations identified within the patient group. In addition to establishing a profile of healthy reference measurements, we have further increased our test specimens to include dual measurements on patients with benign moles and arbitrary diseases. Accordingly, we conducted measurements on 10 patients with benign nevi, where we recorded the response of the sensor when loaded with the nevi, as well as on the adjacent healthy skin, and consequently compared both. The nevi are primarily located on the face and arms of the participants, and they were generally less than 5 mm in diameter. Similarly, we tested the sensor on 7 patients with arbitrary diseases, including Pemphigus Vulgaris, Accessory Tragus, Pyogenic Granuloma, Warts, and Leukemia Cutis. We also differentially measured the response between the diseased lesions and their adjacent healthy counterparts. These experiments allowed us to quantify the difference between healthy skin and cancer within a patient, multiple healthy skin regions within a healthy individual, the difference between benign nevi and arbitrary diseases as well as their adjacent healthy skin, and finally, the variation between all the different sets. Fig. 16(c) and (d) present the dual S_{11} magnitude and phase measurements from two different locations (e.g., two sides of the temples, and two sides of the nose, among others) on all healthy volunteers, respectively. As expected, there were negligible changes in terms of the resonant frequency, the S_{11} magnitude, and the S_{11} phase.

3) *The Distinct Response to Healthy Skin and Cancerous Lesions:* By comparing these measurements from the patient and healthy populations in Fig. 16, the response of the sensor, and equivalently, the nature of the SUT, is manifested as (i) shifts in the resonance frequency of the sensor, and (ii) changes in the magnitude and phase of the sensor's measured S_{11}. For patients, the sensor reacted differently to the cancerous skin lesion and healthy skin, as represented by the shift in resonance frequency, the S_{11} magnitude, and the S_{11} phase. We also present in Fig. 16(e) the difference between the healthy and cancer measurements of each patient across all patients without centering the results at their average shifted resonance frequency to display the measurement variability. Each curve represents the difference curve for one patient, where it is clearly observed that there is a significant and noticeable difference between the S_{11} of the healthy and cancerous skin for each patient. On the other hand, the healthy population exhibited negligible differences in the aforementioned variables. Hence, not only have we identified the key variables indicative of differences within the measured specimen (frequency, magnitude of S_{11}, and phase of S_{11}), but

we have also displayed the existence of distinctive response differences between cancer and healthy skin measurements based on those variables. Such unique differences, their levels, and their associated trends form the basis of our analysis in the coming sections.

B. Skin Cancer Diagnosis

Our objective is to generate an accurate model capable of predicting the malignancy of a suspected lesion based on the differences found within the collected measurement data. Therefore, the obtained S_{11} measurements from the clinical studies are passed onto several data processing stages (as elaborated previously). We rely on the multi-feature nature of the input data (S_{11} measurements obtained at different frequencies) and the measured contrast between healthy skin and diseased skin (within patients) and the measured difference between different healthy regions (within healthy individuals), as well as the differences within individuals having benign nevi and arbitrary diseases to build the model. Consequently, the differential data is then fed into the SVM classifier and then the performance is evaluated.

We analyze the performance of our classifiers by executing the corresponding Receiver Operating Characteristic analysis (ROC analysis) in which we also compute the Area Under the ROC Curve (AUC) to quantify the general performance at all classification thresholds. This analysis is applied to the training and testing data for all three scenarios mentioned previously. Fig. 17(a) presents the ROC curves resulting from the models of the cross-validation training folds corresponding to the 'SC' vs 'BN + AD' scenario along with the mean plotted as well. In Fig. 17(b), we present the mean ROC curves and AUCs corresponding to the analysis executed over all the classifiers that are being applied post cross-validation for the remaining testing data for all three scenarios. The obtained mean AUCs are 1, 0.952, and 0.946, corresponding to the 'SC' vs 'BN + AD', 'SC' vs 'H + BN', and 'SC' vs 'H + BN + AD' scenarios, respectively. These values validate the high performance and capability of our proposed system since both sensitivity and specificity were maintained at high values with insignificant compromise despite utilizing diverse groups corresponding to each scenario (inclusion of benign nevi and arbitrary diseases). The ROCs provide a general overview of the system's performance over many classification thresholds, however, in a clinical setting, a threshold must be chosen to enable prediction utility upon the acquisition of new measurement data. In our approach, we favor the sensitivity metric rather than the specificity, as also adopted in [13]. This is because sensitivity indicates the probability that a diagnosed cancer lesion is truly cancerous, and specificity indicates the probability that a non-cancerous lesion is truly non-cancerous. Hence, a low sensitivity would have dangerous consequences on the patient due to the misdiagnosis of a cancerous lesion as a benign one. For this reason, we focus our efforts on maximizing the sensitivity, without sacrificing the specificity, as it would be safer for the patient to misdiagnose a healthy lesion as cancerous rather than a cancerous lesion as healthy. We also note that, per iteration, the test data was not included in the threshold selection. Table II summarizes the obtained sensitivity and specificity values for all three scenarios.
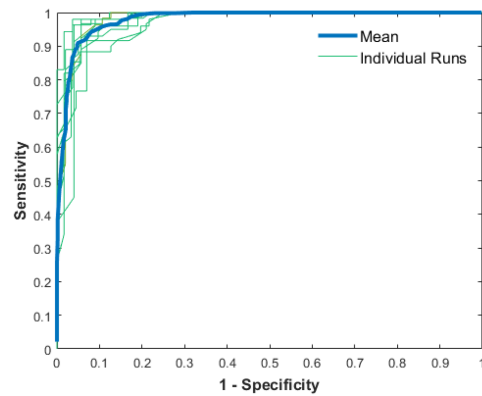
(a)
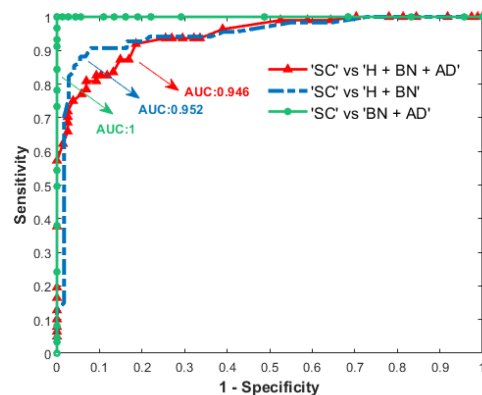
(b)

Fig. 17. (a) represents the ROC curve for the 'SC' vs 'BN + AD' scenario's CV training performance. (b) represents the ROC curves and mean AUCs for the classifiers of all test scenarios based on the performance of the corresponding models resultant from the testing and validation data.

TABLE II
THE CORRESPONDING SENSITIVITY AND SPECIFICITY FOR EACH TEST SCENARIO. SC REPRESENTS SKIN CANCER; H REPRESENTS HEALTHY SKIN; BN REPRESENTS BENIGN NEVI; AD REPRESENTS ARBITRARY DISEASES

'SC' vs. 'H' + 'BN'		'SC' vs. 'BN' + 'AD'		'SC' vs. 'H' + 'BN' + 'AD'	
Sensitivity	Specificity	Sensitivity	Specificity	Sensitivity	Specificity
92%	81.4%	100%	100%	92%	81.4%

Our analysis effectively validates the promising capability of the proposed solution to distinguish cancerous from non-cancerous groups with a sensitivity and specificity of up to 100% and a minimum sensitivity of 92% and specificity of 81.4%, respectively, based on our limited size clinical study. Future wider scale clinical studies will be performed to better understand the efficacy of the proposed solution. In Table III, we present a comparison of the presented work to previous work in the literature. Our primary points of comparison rely on the electromagnetic structure used as well as the stand-alone nature of the proposed system. Importantly, the electromagnetic structure used, such as a near-field sensor [42], a waveguide [17], [18], an antenna [36], or an electrode [13], has a direct influence on the size and cost of the system being proposed. The proposed microstrip-based near-field sensor has the advantage of a more conformal size (31 mm × 11.8 mm × 6 mm) as compared to

TABLE III
LITERATURE COMPARISON

Work	Electromagnetic Structure	Application	Frequency	Technique	Clinical Study	Sensitivity	Specificity	Handheld or Portable
[42]	Near-field sensor	Near-field	13.5 GHz	Sensor + Benchtop VNA	No	NA	NA	NA
[18]	Waveguides	Contact	42 & 70 GHz	Waveguide and Reflectometer	Yes	NA	NA	Yes
[36]	Antennas	Far-field	12 - 110 GHz	Antennas + Benchtop VNA	Yes	97%	98%	No
[13]	Electrode Probe	Contact	1 - 1000 KHz	Electrode and Impedance Spectrometer	Yes	100%	87%	Yes
[17]	Waveguide Probe	Contact	90 - 104 GHz	Waveguide + Benchtop VNA	Yes	NA	NA	No
This work	Near-field sensor	Near-field	4.75 GHz	Sensor and Wave Analyzer Circuit	Yes	92%	81.4%	Yes

the different standard waveguide system assemblies along with their corresponding VNAs. Additionally, the proposed approach is also considered application-oriented since no special setups are required. Most of the proposed systems in the literature require stable fixtures for mounting the sensing device or special alignment accommodations as in the case of the antenna-based transmission systems. To the contrary, the adoption of our proposed system in clinics is smoother and easier. While the systems in [13], [36] presented higher sensitivity (97% and 100%) and specificity (98% and 87%) than the proposed system (92% and 81.4%), we provide a fully handheld solution. Additionally, the work in [18] provides a handheld system composed of a waveguide and a diode detector to output the magnitude of the reflected signal, however it does not measure phase values (which contain additional valuable information that can supplement the magnitude values) as well as a statistical model is not presented for diagnostic output.

V. CONCLUSION

The presented system establishes a unique and innovative platform that successfully integrates EM-based sensing for dermatology diagnostics. The combination of several sensor design decisions tailored for malignant lesion detection and the multi-feature statistical analysis methods enhanced our sensitivity. Our findings attest to our system's ability to electromagnetically interrogate suspected skin lesions non-invasively. There is a clear need for a quick point-of-care device capable of diagnosing skin cancer, especially because delays in skin cancer screening cause the disease to evolve, potentially spreading into other tissues and resulting in dangerous health complications.

As for clinical utility, the sensing tip is particularly useful for surgeons removing cancerous skin lesions. In the traditional wide-margin excision method, "normal skin" surgical margins need to be drawn around the skin cancer and removed. They vary in size from 3 mm to 20 mm beyond the visible tumor size. This is done to make sure all the cancer is removed as cancer cells often extend beyond what the physician clinically sees. Due to its fine sensing tip, the proposed "pen-like" device can accurately determine small and large tumors' malignancy, effectively identifying the boundaries of cancer both qualitatively and quantitatively, as proven by our clinical studies. Similarly, this also confers a massive advantage to patients undergoing Moh's Micrographic Surgery where successive excisions from the suspected lesions are often required to ensure the complete removal of cancer. The sensor can detect the actual limit of the tumor much more accurately when compared to the conventional methods of skin cancer assessment. Hence, the number of stages (or re-excisions)

needed can be minimized, therefore allowing the surgeon to draw the cancer limit more precisely from the beginning. Such an advantage reduces the duration of the procedure as well as the risk of potential disfigurement in sensitive regions and the risk of tumor recurrence. In addition, the frequency of operation, being within the microwave range, results in a significantly reduced design cost of the RF components required for the wave analyzer system when compared to the design cost of components that operate at mm-wave frequencies and beyond. Moreover, the proposed device exhibits several advantageous features when compared to other efforts within the literature, such as portability, non-constraining, and low-cost. The results from our limited population studies are highly encouraging, which drives towards up-scaled and more extensive clinical testing in the future.

REFERENCES

[1] K. Brind'Amour, "All about common skin disorders," Aug. 30, 2022. [Online]. Available: https://www.healthline.com/health/skin-disorders

[2] "Skin cancer (Non-Melanoma) - Introduction cancer.net," Jun. 22, 2022. [Online]. Available: https://www.cancer.net/cancer-types/skin-cancer-non-melanoma/introduction

[3] "What are basal and squamous cell skin cancers? —Types of skin cancer," Jul. 26, 2019. [Online]. Available: https://www.cancer.org/cancer/basal-and-squamous-cell-skin-cancer/about/what-is-basal-and-squamous-cell.html

[4] "Radiation: Ultraviolet (UV) radiation and skin cancer," Oct. 16, 2017. [Online]. Available: https://www.who.int/news-room/q-a-detail/radiation-ultraviolet-(uv)-radiation-and-skin-cancer

[5] "Early detection. The skin cancer foundation," Jan. 29, 2018. [Online]. Available: https://www.skincancer.org/early-detection/

[6] "Skin cancer - Symptoms and causes. Mayo Clinic," Dec. 5, 2022. [Online]. Available: https://www.mayoclinic.org/diseases-conditions/skin-cancer/symptoms-causes/syc-20377605

[7] "Melanoma warning signs and images. The skin cancer foundation," Jan. 1, 2021. [Online]. Available: https://www.skincancer.org/skin-cancer-information/melanoma/melanoma-warning-signs-and-images/

[8] "Not my face! The skin cancer foundation," Nov. 1, 2017. [Online]. Available: https://www.skincancer.org/blog/not-my-face/

[9] K. Abhishek and N. Khunger, "Complications of skin biopsy," J. Cutan. Aesthetic Surg., vol. 8, no. 4, pp. 239–241, 2015. [Online]. Available: https://www.ncbi.nlm.nih.gov/pmc/articles/PMC4728909/

[10] B. Lindelöf and M. A. Hedblad, "Accuracy in the clinical diagnosis and pattern of malignant melanoma at a dermatological clinic," J. Dermatol., vol. 21, no. 7, pp. 461–464, 1994.

[11] C. A. Morton and R. M. Mackie, "Clinical accuracy of the diagnosis of cutaneous malignant melanoma," Brit. J. Dermatol., vol. 138, no. 2, pp. 283–287, 1998.

[12] M. D. Corbo and J. Wismer, "Agreement between dermatologists and primary care practitioners in the diagnosis of malignant melanoma: Review of the literature," J. Cutan. Med. Surg., vol. 16, no. 5, pp. 306–310, Sep./Oct. 2012.

[13] P. Aberg, I. Nicander, J. Hansson, P. Geladi, U. Holmgren, and S. Ollmar, "Skin cancer identification using multifrequency electrical impedance–A potential screening tool," IEEE Trans. Bio- Med. Eng., vol. 51, no. 12, pp. 2097–2102, Dec. 2004.

[14] T. J. Brinker et al., "Skin cancer classification using convolutional neural networks: Systematic review," *J. Med. Internet Res.*, vol. 20, no. 10, 2018, Art. no. e11936. [Online]. Available: https://www.jmir.org/2018/10/e11936/

[15] "Using deep learning to inform differential diagnoses of skin diseases. Google AI Blog," Sep. 13, 2019. [Online]. Available: http://ai.googleblog.com/2019/09/using-deep-learning-to-inform.html

[16] M. Goyal, T. Knackstedt, S. Yan, and S. Hassanpour, "Artificial intelligence-based image classification methods for diagnosis of skin cancer: Challenges and opportunities," *Comput. Biol. Med.*, vol. 127, 2020, Art. no. 104065. [Online]. Available: https://www.sciencedirect.com/science/article/pii/S0010482520303966

[17] F. Töpfer, S. Dudorov, and J. Oberhammer, "Millimeter-wave near-field probe designed for high-resolution skin cancer diagnosis," *IEEE Trans. Microw. Theory Techn.*, vol. 63, no. 6, pp. 2050–2059, Jun. 2015.

[18] A. Taeb, S. Gigoyan, and S. Safavi-Naeini, "Millimetre-wave waveguide reflectometers for early detection of skin cancer," *IET Microw., Antennas Propag.*, vol. 7, no. 14, pp. 1182–1186, Nov. 2013.

[19] A. Rahman, A. K. Rahman, and B. Rao, "Early detection of skin cancer via terahertz spectral profiling and 3D imaging," *Biosensors Bioelectron.*, vol. 82, pp. 64–70, 2016.

[20] J. L. Schepps and K. R. Foster, "The UHF and microwave dielectric properties of normal and tumour tissues: Variation in dielectric properties with tissue water content," *Phys. Med. Biol.*, vol. 25, no. 6, pp. 1149–1159, 1980, doi: 10.1088/0031-9155/25/6/012.

[21] M. Lazebnik et al., "A large-scale study of the ultrawideband microwave dielectric properties of normal, benign and malignant breast tissues obtained from cancer surgeries," *Phys. Med. Biol.*, vol. 52, no. 20, pp. 6093–6115, 2007.

[22] A. Mirbeik-Sabzevari, R. Ashinoff, and N. Tavassolian, "Ultra-wideband millimeter-wave dielectric characteristics of freshly excised normal and malignant human skin tissues," *IEEE Trans. Biomed. Eng.*, vol. 65, no. 6, pp. 1320–1329, Jun. 2018.

[23] F. Kazemi, F. Mohanna, and J. Ahmadi-Shokouh, "Detection of biological abnormalities using a near-field microwave microscope," *Int. J. Microw. Wireless Technol.*, vol. 10, no. 8, pp. 933–941, 2018.

[24] A. Mirbeik-Sabzevari, R. Ashinoff, and N. Tavassolian, "Ultra-wideband millimeter-wave dielectric characteristics of freshly excised normal and malignant human skin tissues," *IEEE Trans. Biomed. Eng.*, vol. 65, no. 6, pp. 1320–1329, Jun. 2018.

[25] M. Phillips et al., "Assessment of accuracy of an artificial intelligence algorithm to detect melanoma in images of skin lesions," *J. Amer. Med. Assoc. Netw. Open*, vol. 2, no. 10, 2019, Art. no. e1913436, doi: 10.1001/jamanetworkopen.2019.13436.

[26] A. Esteva et al., "Dermatologist-level classification of skin cancer with deep neural networks," *Nature*, vol. 542, no. 7639, pp. 115–118, 2017, doi: 10.1038/nature21056.

[27] X. Du-Harpur et al., "Clinically relevant vulnerabilities of deep machine learning systems for skin cancer diagnosis," *J. Invest. Dermatol.*, vol. 141, no. 4, pp. 916–920, 2021. [Online]. Available: https://pubmed.ncbi.nlm.nih.gov/32931808

[28] "Papers with code - ISIC 2018 task 3 dataset," Aug. 12, 2021. [Online]. Available: https://paperswithcode.com/dataset/isic-2018-task-3

[29] C. Gabriel, S. Gabriel, and E. Corthout, "The dielectric properties of biological tissues: I literature survey," *Phys. Med. Biol.*, vol. 41, no. 11, pp. 2231–2249, 1996, doi: 10.1088/0031-9155/41/11/001.

[30] D. M. Pozar, *Microwave Engineering*. Hoboken, NJ, USA: Wiley, 2012.

[31] L. Chen, C. Ong, C. Neo, V. Varadan, and V. Varadan, *Microwave Electronics: Measurement and Materials Characterization*. Hoboken, NJ, USA:Wiley, 2004. [Online]. Available: https://books.google.com.lb/books?id=1vmUdUXlBNIC

[32] S. Gabriel, R. W. Lau, and C. Gabriel, "The dielectric properties of biological tissues: II. measurements in the frequency range 10 Hz to 20 GHz," *Phys. Med. Biol.*, vol. 41, no. 11, pp. 2251–2269, 1996, doi: 10.1088/0031-9155/41/11/002.

[33] G. Martinsen, S. Grimnes, and H. Schwan, "Interface phenomena and dielectric properties of biological tissue. undefined," 2022. [Online]. Available: https://www.mn.uio.no/fysikk/english/research/projects/bioimpedance/publications/papers/encyclop.pdf

[34] S. Gabriel, R. W. Lau, and C. Gabriel, "The dielectric properties of biological tissues: III. Parametric models for the dielectric spectrum of tissues," *Phys. Med. Biol.*, vol. 41, no. 11, pp. 2271–2293, 1996, doi: 10.1088/0031-9155/41/11/003.

[35] A. Mirbeik-Sabzevari, E. Oppelaar, R. Ashinoff, and N. Tavassolian, "High-contrast, low-cost, 3-D visualization of skin cancer using ultra-high-resolution millimeter-wave imaging," *IEEE Trans. Med. Imag.*, vol. 38, no. 9, pp. 2188–2197, Sep. 2019.

[36] A. Mirbeik, R. Ashinoff, T. Jong, A. Aued, and N. Tavassolian, "Real-time high-resolution millimeter-wave imaging for in-vivo skin cancer diagnosis," *Sci. Rep.*, vol. 12, no. 1, 2022, Art. no. 4971. [Online]. Available: https://www.nature.com/articles/s41598-022-09047-6

[37] "RT/duroid 5880 laminates - rogers corporation," May 25, 2018. [Online]. Available: https://www.rogerscorp.com/advanced-electronics-solutions/rt-duroid-laminates/rt-duroid-5880-laminates

[38] "ANSYS HFSS: High frequency electromagnetic field simulation software," Jan. 5, 2022. [Online]. Available: https://www.ansys.com/products/electronics/ansys-hfss

[39] "Radiofrequency (RF) Radiation," Oct. 28, 2022. [Online]. Available: https://www.cancer.org/cancer/cancer-causes/radiation-exposure/radiofrequency-radiation.html

[40] "Radio frequency safety. federal communications commission," Aug. 31, 2020. [Online]. Available: https://www.fcc.gov/general/radio-frequency-safety-0

[41] M. Tabib-Azar, J. L. Katz, and LeClair, "Evanescent microwaves: A novel super-resolution noncontact nondestructive imaging technique for biological applications," *IEEE Trans. Instrum. Meas.*, vol. 48, no. 6, pp. 1111–1116, Dec. 1999.

[42] F. Kazemi, F. Mohanna, and J. Ahmadi-Shokouh, "Nondestructive high-resolution microwave imaging of biomaterials and biological tissues," *AEU - Int. J. Electron. Commun.*, vol. 84, pp. 177–185, 2018. [Online]. Available: http://www.sciencedirect.com/science/article/pii/S1434841117314619

[43] "N9923a fieldfox handheld rf vector network analyzer, 4 GHz and 6 GHz– keysight," Oct. 1, 2021. [Online]. Available: https://www.keysight.com/en/pdx-x201782-pn-N9923A/fieldfox-handheld-rf-vector-network-analyzer-4-ghz-and-6-ghz?cc=LB&lc=eng

[44] "Downloads–KiCad EDA," Jan. 13, 2019. [Online]. Available: https://downloads.kicad.org/kicad/windows/explore/stable

[45] "PCB Prototype-JLCPCB," Nov. 29, 2022. [Online]. Available: https://jlcpcb.com/quote/pcbOrderFaq/PCB%20Stackup

[46] Keysight, "Pathwave advanced design system (ads). keysight," Oct. 1, 2021. [Online]. Available: https://www.keysight.com/zz/en/products/software/pathwave-design-software/pathwave-advanced-design-system.html

[47] Y. Shen, C. Wu, C. Liu, Y. Wu, and N. Xiong, "Oriented feature selection SVM applied to cancer prediction in precision medicine," *IEEE Access*, vol. 6, pp. 48510–48521, 2018.

[48] Z. Huang, C. Yang, X. Chen, K. Huang, and Y. Xie, "Adaptive over-sampling method for classification with application to imbalanced datasets in aluminum electrolysis," *Neural Comput. Appl.*, vol. 32, no. 11, pp. 7183–7199, 2020, doi: 10.1007/s00521-019-04208-7.

[49] E. Zafiropoulos, I. Maglogiannis, and I. Anagnostopoulos, "A Support Vector Machine Approach to Breast Cancer Diagnosis and Prognosis," in *Artificial Intelligence Applications and Innovations*(IFIP International Federation for Information Processing Series), I. Maglogiannis, K. Karpouzis, and M. Bramer, Eds. Berlin, Germany:Springer, 2006, pp. 500–507.

[50] H.-J. Chiu, T.-H. S. Li, and P.-H. Kuo, "Breast cancer–detection system using PCA, multilayer perceptron, transfer learning, and support vector machine," *IEEE Access*, vol. 8, pp. 204309–204324, 2020.

[51] "Sequential feature selection - MATLAB & simulink," Apr. 15, 2022. [Online]. Available: https://www.mathworks.com/help/stats/sequential-feature-selection.html

[52] A. Fernandez, S. Garcia, F. Herrera, and N. V. Chawla, "SMOTE for learning from imbalanced data: Progress and challenges, marking the 15-year anniversary," *J. Artif. Intell. Res.*, vol. 61, pp. 863–905, 2018. [Online]. Available: https://www.jair.org/index.php/jair/article/view/11192

[53] M. Alghamdi, M. Al-Mallah, S. Keteyian, C. Brawner, J. Ehrman, and S. Sakr, "Predicting diabetes mellitus using SMOTE and ensemble machine learning approach: The henry ford ExercIse testing (FIT) project," *PLoS One*, vol. 12, no. 7, 2017, Art. no. e0179805. [Online]. Available: https://www.ncbi.nlm.nih.gov/pmc/articles/PMC5524285/

[54] S. F. Abdoh, M. A. Rizka, and F. A. Maghraby, "Cervical cancer diagnosis using random forest classifier with SMOTE and feature reduction techniques," *IEEE Access*, vol. 6, pp. 59475–59485, 2018.

[55] W. Wiharto, H. Kusnanto, and H. Herianto, "Intelligence system for diagnosis level of coronary heart disease with K-star algorithm," *Healthcare Inform. Res.*, vol. 22, no. 1, pp. 30–38, 2016. [Online]. Available: https://www.ncbi.nlm.nih.gov/pmc/articles/PMC4756056/

[56] "Federalwide assurance," Aug. 31, 2023. [Online]. Available: https://www.aub.edu.lb/irb/Pages/federalwideassurance.aspx

[57] "Mohs surgery - mayo clinic," Feb. 1, 2023. [Online]. Available: https://www.mayoclinic.org/tests-procedures/mohs-surgery/about/pac-20385222

[58] D. Huber, M. Talary, F. Dewarrat, and A. Caduff, "The compensation of perturbing temperature fluctuation in glucose monitoring technologies based on impedance spectroscopy," *Med. Biol. Eng. Comput.*, vol. 45, no. 9, pp. 863–876, 2007.

[59] D. A. Pollacco, L. Farina, P. S. Wismayer, L. Farrugia, and C. V. Sammut, "Characterization of the dielectric properties of biological tissues and their correlation to tissue hydration," *IEEE Trans. Dielectrics Elect. Insul.*, vol. 25, no. 6, pp. 2191–2197, Dec. 2018.

[60] R. J. Halter et al., "The correlation of in vivo and ex vivo tissue dielectric properties to validate electromagnetic breast imaging: Initial clinical experience," *Physiol. Meas.*, vol. 30, no. 6, pp. S121–S136, 2009.

[61] L. Farrugia, P. S. Wismayer, L. Z. Mangion, and C. V. Sammut, "Accurate in vivo dielectric properties of liver from 500 MHz to 40 GHz and their correlation to ex vivo measurements," *Electromagn. Biol. Med.*, vol. 35, no. 4, pp. 365–373, 2016, doi: 10.3109/15368378.2015.1120221.

[62] S. Salahuddin, A. L. Gioia, M. A. Elahi, E. Porter, M. O'Halloran, and A. Shahzad, "Comparison of in-vivo and ex-vivo dielectric properties of biological tissues," in *Proc. IEEE Int. Conf. Electromagn. Adv. Appl.*, 2017, pp. 582–585.

Rouwaida Kanj (Senior Member, IEEE) received the M.S. and Ph.D. degrees in electrical engineering from the University of Illinois Urbana-Champaign, Champaign, IL, USA, in 2000 and 2004, respectively. She is currently a tenured Associate Professor with the American University of Beirut, Beirut, Lebanon. From 2004 to 2012 she was a Research Staff Member with IBM Austin Research Laboratory, Austin, TX, USA. In 2022, she joined Synopsys R&D Reliability Team as a Member of Technical Staff. She is the author of more than 90 technical papers, 38 issued U.S. patents and several pending patents. Her research interests include advanced algorithmic research and development and smart analytics methodologies for Design for manufacturability reliability and yield with emphasis on statistical analysis, optimization and rare fail event estimation for microprocessor memory designs along with machine learning applications for very large scale integration. More recently, she is also involved in memristor-based memory design and reliability and the design of reliable circuits and systems for healthcare and in-memory compute. This is in addition to her earlier work on noise modeling and characterization of CMOS designs. Dr. Kanj was the recipient of three IBM Ph.D. Fellowships, an outstanding Technical Achievement Award and six Invention Plateau awards from IBM, prestigious IEEE/ACM WILLIAM J. MCCALLA ICCAD Best Paper Award in 2009, and two IEEE ISQED best paper awards in 2006 and 2014, and IEEE ICM best paper award in 2020. In 2018, her work on statistical yield analysis methodology was nominated for the ACM/IEEE Richard Newton Award. She is currently serves or chairs on the technical program committees of several prestigious IEEE conferences. She is also a Peer-Reviewer of many prestigious journals. She was also the recipient of the American University of Beirut Teaching Excellence Award in 2021.

Nader Shafi received the Bachelor of Engineering degree in computer and communications engineering from American University of Beirut, Beirut, Lebanon, in 2018, and the master's degree (with high distinction) in electrical and computer Engineering from the American University of Beirutin, in 2020, where he specialized in radio-frequency and applied electromagnetics. He is currently a Research Associate with the American University of Beirut, EMPACT Lab, where he continues to explore new horizons to effectively integrate innovative engineering solutions to be used in highly compact wearable sensors. He is also the Co-founder of SkanMD, a startup that aims to improve dermatology diagnostics through RF technology. In 2021, he was named as one of the top innovators under 35 in the MENA region by the MIT technology review.

Joseph Costantine (Senior Member, IEEE) received the bachelor's degree from the second branch of the Faculty of Engineering, Lebanese University, Beirut, Lebanon, in 2004, and the master's (M.E.) degree from the American University of Beirut, Beirut, in 2006, and the Doctorate degree from The University of New Mexico, Albuquerque, NM, USA, in 2009. He is currently an Associate Professor with the Electrical and Computer Engineering Department and has been a World Economic Forum young Scientist since 2020. He has 11 Provisional and Full U.S. patents. He has authored or coauthored so far two books, two book chapters, and more than 180 Journal and conference papers. His research interests include reconfigurable antennas, cognitive radio, RF energy harvesting systems, antennas and rectennas for IoT devices, RF systems for biomedical devices, wireless characterization of dielectric material, and deployable antennas for small satellites. He has been a Senior Member of the IEEE since June 2019, an Associate Editor for the IEEE ANTENNAS AND WIRELESS PROPAGATION LETTERS since July 2018, and an Associate Editor for the IEEE TRANSACTIONS ON ANTENNAS AND PROPAGATION since September 2022. He was the recipient of many awards and honors throughout his career, including the 2008 IEEE Albuquerque Chapter Outstanding Graduate Award, three-year (2011-2013) summer Faculty Fellowship with Kirtland space vehicles directorate in NM, USA, 2017 first prize at the Idea-thon of international healthcare industry forum, 2019 excellence in teaching award from American University of Beirut, 2018 and 2020 STC Science and Technology Innovation Awards, and 2020 distinguished young Alumni Award from the School of Engineering at the University of New Mexico.

Youssef Tawk (Senior Member, IEEE) received the Bachelor of Engineering degree (with the highest distinction) from Notre Dame University, Louaize, Zouk Mosbeh, Lebanon, in Fall 2006, the Master's in Engineering degree from the American University of Beirut, Beirut, Lebanon, in 2007, and the Ph.D. degree from The University of New Mexico, Albuquerque, NM, USA, in 2011. He is currently an Associate Professor with the Electrical and Computer Engineering Department, American University of Beirut. He was the valedictorian of his graduating class with Notre Dame University, Louaize. He has more than 180 IEEE journals and conference papers many of which received finalist positions and honorable mentions in several paper contests. He is the co-author of two books and two book chapters and co-inventor of eight provisional and full U.S. patents. His research interests include antennas and modern communication systems for IoT, 5G and beyond, reconfigurable antennas and RF systems for microwave and millimeter-wave applications, cognitive radio, optically controlled antennas and RF components, phased antennas arrays, and reconfigurable phase shifters based on advanced additive manufacturing techniques. Throughout his education and career, Dr. Tawk was the recipient of many awards and honors, such as the 2021 IEEE Donald Dudley Jr. Teaching Award from the IEEE Antennas and Propagation Society, Science and Technology Innovation Award for his patents on deployable and 3D printed antenna systems in 2020, on reconfigurable filtennas in 2018, and on innovating optically controlled antenna systems in 2014. In addition, he was also the IEEE Albuquerque Chapter Outstanding Graduate Award in 2011. He has been a Senior Member of the IEEE since February 2020, an Associate Editor for *Wiley Microwave and Optical Technology Letter* since September 2019, and an Associate Editor for the IEEE TRANSACTIONS ON ANTENNAS AND PROPAGATION since September 2022.
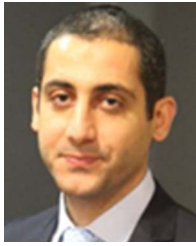
Ali H. Ramadan (Member, IEEE) received the Ph.D. degree in electrical and computer engineering from the American University of Beirut, Beirut, Lebanon, in 2014. In 2010, he joined the Cognitive Radio Research Group, Electrical and Computer Engineering Department, The University of New Mexico, Albuquerque, NM, USA, where he was a Ph.D. Exchange Research Scholar from 2010 to 2013. In 2014, he was a Postdoctoral Fellow with the Electrical and Computer Engineering Department, American University of Beirut, where he held a Research Associate position, in 2017. He is currently an Assistant Professor with the Electrical Engineering Department, Fahad Bin Sultan University, Tabuk, Saudi Arabia. His research interests include wireless power transfer, bio-electromagnetics, reconfigurable RF front-end transceivers for Internet of Things applications, and phased antenna arrays.

Mazen Kurban is currently a Dermatologist and an American Board Certified in Clinical Molecular Genetics. He is also a Tenured Professor of dermatology, biochemistry and molecular genetics with the American University of Beirut Medical Center, Beirut, Lebanon, and an Adjunct Professor with the Department of Genetics and Genomics, Hamad University, Doha, Qatar. He has more than 175 publications in clinical, basic science, and translational research in the field of dermatology and genetics. He is the current Vice President of the Lebanese Society of Dermatology. He was the recipient of several national and international awards.
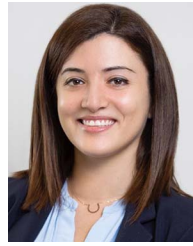
Jihane Abou Rahal received the medical degree from the American University of Beirut, Beirut, Lebanon, in 2015, and an Inter-University Diploma in surgical dermatology. She is currently an Assistant Professor of dermatology with the American University of Beirut - Medical Center (AUBMC), Beirut, Lebanon, and the Program Director of the Dermatology Residency Program. She has a sub specialty in procedural dermatology and mohs micrographic surgery with a particular interest in skin cancer. She established the Mohs micrographic surgery services with AUBMC, in 2017. After earning her medical degree and dermatology residency from the American University of Beirut in 2015, she sub-specialized in surgical dermatology and Mohs surgery with the University Hospital of Bordeaux, Bordeaux, France, in 2016. Her training focused on dermatological oncological and non-oncological surgeries and reconstructions, and lasers and other less invasive procedures. She is a Certified Member of the European Society of Mohs Surgeons.
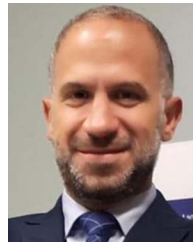
Assaad A. Eid received the Doctorate degree in metabolism and endocrinology from Claude Bernard University, France, in 2006. He completed four years of postdoctoral training in medicine/nephrology with the University of Texas Health Science Center in San Antonio, TX, USA, in 2010. He is currently the Associate Dean for basic/translational research and graduate studies with the Faculty of Medicine, American University of Beirut, Beirut, Lebanon. He is also the I/Chairperson of the Department of Anatomy Cell Biology and Physiological Sciences at the same faculty and the Director of the AUB Diabetes, American University of Beirut Medical Center, Beirut. He is an internationally renowned Investigator with a focus on complications of diabetes, and his research has contributed to identifying several signaling pathways involved in the development of diabetic complications. He has authored or coauthored in top-tier journals, secured extramural and intramural research grants, and co-founded two startups. He was the recipient of several national and international awards, including the Lebanese National Order of Merit.